buildings

MDPI

Article

Load-Bearing Performance of Steel–Concrete Composite Reticulated Shell Segments Based on the Secondary Service Life Concept

Li Xing *, Gang Wei and Lan Wang

Department of Civil Engineering, Hangzhou City University, Hangzhou 310015, China; weig@hzcu.edu.cn (G.W.)
* Correspondence: xingli@hzcu.edu.cn

Abstract

Shield tunnels enter the operation and maintenance stage, ensuring the long-term safety of segmental linings has become a critical challenge. To overcome the limitations of traditional passive repair, this study introduces novel steel–concrete composite reticulated shell segments (SCRSs) based on the secondary service life concept. A scaled-model surcharge test was conducted to evaluate the baseline performance and failure mechanisms of unstrengthened segments (S-CN). Subsequently, a secondary concrete layer was cast inside the deformed segments (S-CR) to assess post-damage structural recovery, supported by theoretical ring mechanics analyses. Experimental results indicate that the unstrengthened SCRS exhibits pronounced load-bearing capacity and ductility, characterized by a progressive three-stage response encompassing the elastic stage, yield plateau, and post-yield stage; the test was terminated at a load of 141.95 kN with the curve still ascending, so this value represents a terminal load and a lower bound on the ultimate capacity. This behavior stems from the sequential engagement of outer reinforcement and the inner steel framework, providing clear deformation warnings prior to structural failure. Furthermore, casting the secondary concrete layer enhanced both the stiffness and the load-bearing capacity of the deformed specimen, which sustained a maximum total load of 203.14 kN; this value is a local failure threshold governed by concrete crushing beneath the concentrated loading heads rather than a structural peak load. The as-built specimens were fabricated from commercially processed steel members and hand-mixed concrete, and their measured material properties (a measured ultimate tensile strength of about 240–400 MPa for the steel, varying between two test batches; a cubic compressive strength of 27 MPa for the concrete) were used throughout the analysis. The experimental data support the feasibility of the secondary service life concept as a proof-of-concept study of the segment body, within the limitations of a single scaled specimen and short-term monotonic loading. This composite design offers a potential pathway for shifting shield tunnel linings from reactive repair to proactive, whole-life management.

Keywords: shield tunnel; steel–concrete composite; reticulated shell segments; secondary service life concept; load-bearing performance; scaled-model test; structural strengthening

Check for updates

Academic Editor: Vipul Patel

Received: 30 September 2026
Revised: 26 October 2026
Accepted: 28 October 2026
Published: 29 October 2026

Copyright: © 2026 by the authors. Licensee MDPI, Basel, Switzerland. This article is an open access article distributed under the terms and conditions of the Creative Commons Attribution (CC BY) license.

1. Introduction

With the operational mileage of urban rail transit in China exceeding 13,000 km [1], shield tunnels have transitioned from a large-scale construction phase to an operation and maintenance (O&M)-dominated phase. Consequently, ensuring the structural safety

of segmental linings has become a core issue for the resilience of urban underground lifelines [2,3]. As the primary permanent load-bearing components, segments frequently suffer from distress—such as joint dislocation, cracking-induced leakage, and convergence deformation—under the coupled effects of high water/earth pressures and complex service loads [4–7]. Statistically, crack-related defects account for over 60% of all reported cases [8]. Furthermore, the progressive collapse accident of the Sasago Tunnel in Japan, triggered by connector fatigue failure [9], highlights the urgency of safeguarding the whole-life safety of segmental structures.

To address performance degradation, the engineering community has developed various technologies, including inner steel plate linings, fiber-reinforced polymer (FRP) wrapping, micro-disturbance grouting, and steel–concrete composite strengthening [10–12]. Recent international studies have investigated composite strengthening systems for in-service segmental linings, covering full-scale experiments on deformed linings [13], numerical analysis [14], and the behavior of strengthened segmental joints [15]. However, these methods share a common limitation: they rely on post-event passive repair. They can only be implemented after visible damage emerges, failing to intervene proactively during early deterioration. More critically, strengthening operations often require traffic interruption, face severe spatial constraints, and depend heavily on the interfacial bonding quality between old and new materials—meaning any debonding can lead to system failure [16–18]. Ultimately, this reactive approach falls short of extending the true design service life.

Inspired by the concept of secondary service life, we integrate structural performance enhancement, and future maintenance demands directly into the initial design stage. By reserving spatial allowances and designing synergistic interfaces, segments can undergo secondary construction to restore load-bearing capacity after their primary service life concludes. This paradigm shifts structural strengthening from an emergency fix to a proactive, planned strategy.

At the implementation level, steel–concrete composite reticulated shell segments (SCRSs) offer a promising carrier for this concept. While recent studies have explored novel materials—such as steel fiber-reinforced concrete (SFRC) [19–21], BFRP/GFRP [22,23], and engineered geopolymer composites (EGC) [24]—to upgrade segment performance, they remain confined to material-level substitutions. To date, no study has introduced a spatial reticulated shell structure into segment design to build SCRSs, nor has anyone systematically investigated their load-bearing mechanisms and strengthening potential. This study aims to bridge this gap.

Specifically, the following three research gaps urgently require addressing: (1) the structural feasibility and mechanical mechanisms of the integrated design of reticulated shells and segments remain unclear; (2) there is a lack of physical verification regarding the implementation pathway of the secondary service life concept in novel segments; and (3) experimental data supporting the secondary strengthening effectiveness of damaged novel segments are currently insufficient.

Therefore, this paper proposes and evaluates novel steel–concrete composite reticulated shell segments (SCRSs) based on the secondary service life concept. Scaled model surcharge loading tests are conducted to systematically investigate their load-bearing performance, mechanical behavior, and failure modes. Furthermore, secondary strengthening tests are performed on damaged segments to assess their capacity recovery. As a proof-of-concept study of the segment body, this work aims to provide experimental evidence and theoretical support for shifting shield tunnel segments from passive repair to active design. (Note: The technical schemes presented in this paper have been filed for Chinese invention patents under Application Nos. 202410348086.0 and 202411391228.8.)

2. Structural Design

2.1. Design Concept

Traditional reinforced concrete (RC) segments are designed as single-use structures, making proactive intervention difficult once performance degrades during service. To address this, the secondary service life concept is introduced, framing the segment as a load-bearing system with inherent renewal capacity.

The core of this concept relies on a dual load-bearing mechanism. The outer RC layer sustains water and earth pressures during the primary service stage to ensure structural integrity. Meanwhile, the inner steel reticulated shell not only shares operational loads but also leverages its open spatial configuration to provide a natural casting channel, bonding interface, and shear connection for a subsequent cast-in-place concrete secondary lining. Thus, the exposed steel skeleton functions as both a primary load-bearing component and the connecting medium for the "segment–lining" composite system during later strengthening.

When long-term degradation occurs, costly demolition and replacement can be avoided. By simply casting a secondary concrete layer internally, a composite system is formed through the embedding and interlocking action of the steel reticulated shell, effectively restoring or enhancing load-bearing performance. This design transforms shield segments from single-use components into structural units with built-in secondary strengthening potential.

Loading pathway and failure modes: Under service, the external water and earth pressures are taken up by the outer RC shell and transferred to the inner reticulated shell through the embedded connection plates and the bolted spherical joints of the prototype (the tested specimen used direct welding instead; Section 3.1), and are then distributed circumferentially and longitudinally by the upper chords, web members and lower chords. The outer concrete carries the compression while the steel shell carries the tension, and after the concrete cracks the tensile action is transferred to the steel skeleton, which acts as a second line of defense. The corresponding failure modes were identified experimentally (Section 4.1): the unstrengthened segment fails in a ductile, flexure-tension-governed mode with a pronounced yield plateau and a clear deformation warning, whereas the strengthened segment fails by local compression crushing beneath the concentrated loading heads, the flexural capacity of the composite section not being exhausted.

2.2. Geometric Configuration of the Novel Segment

The proposed steel–concrete composite reticulated shell segment (SCRS) consists of two primary components: an outer reinforced concrete layer and an inner double-layer steel reticulated shell (Figure 1). The upper and lower chords of the shell are tied with bolted spherical joints, which not only streamline on-site assembly but also provide practical convenience for future member inspection and replacement.

The detailed configuration of the bolted spherical joints is shown in Figure 2. The upper spheres are welded to bearing base plates, which are anchored directly to the internal reinforcement mesh within the precast concrete blocks. This pre-assembled unit is cast integrally to ensure reliable anchorage. Each block features a fully welded reinforcement skeleton to guarantee local load-bearing capacity. Multiple blocks are subsequently bolted together to form a complete segmental ring, which works jointly with the internal shell to establish a high-performance composite system.

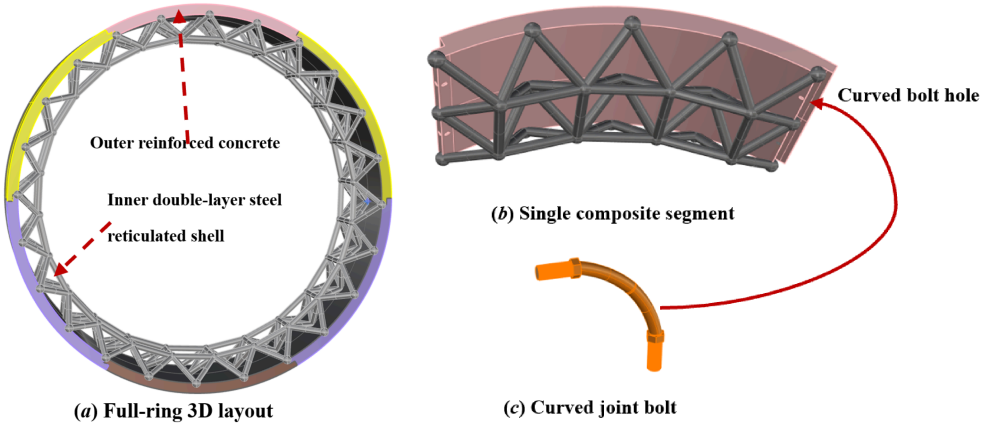


Figure 1. Geometric configuration and components of the SCRS lining system: (**a**) full-ring 3D layout with the key, adjacent and standard blocks colour-coded; (**b**) single composite segment with the curved bolt hole; (**c**) curved joint bolt.

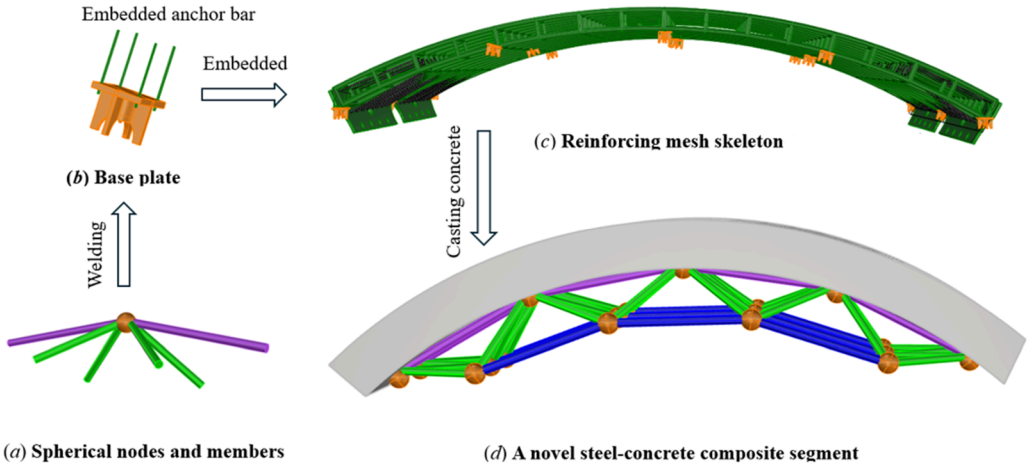


Figure 2. Schematic diagram of the SCRS connections.

This structural design follows the load-bearing principles of composite systems. By replacing the inner concrete with a reticulated shell, the concrete thickness and overall self-weight are reduced without compromising load capacity. Meanwhile, the combined action of steel in tension and concrete in compression significantly enhances load performance and structural stability. The open configuration of the reticulated shell also improves internal space utilization and provides favorable seismic behavior. Crucially, upon reaching the end of its design life, a secondary concrete layer can be cast inside to fully encase the shell, forming an integrated load-bearing system. This enables performance restoration without reducing the original inner clearance, thus granting the segment a secondary service life.

2.3. Analysis of Structural Load-Bearing Mechanism

The load transfer path of the new segment is illustrated in Figure 3: external water and earth pressures → outer RC shell → embedded connection plates → bolted spherical joints → inner steel reticulated shell (upper chords → web members → lower chords). The outer concrete shell acts as the primary compression-bearing component, taking up external loads and transferring them to the steel shell through the embedded plates. Serving as the internal skeleton, the reticulated shell distributes these loads circumferentially and longitudinally to establish a spatial load-bearing system. Effective load transfer between the steel shell and outer concrete is achieved by welding the spherical joints to the embedded plates, ensuring that both materials work cooperatively rather than independently.

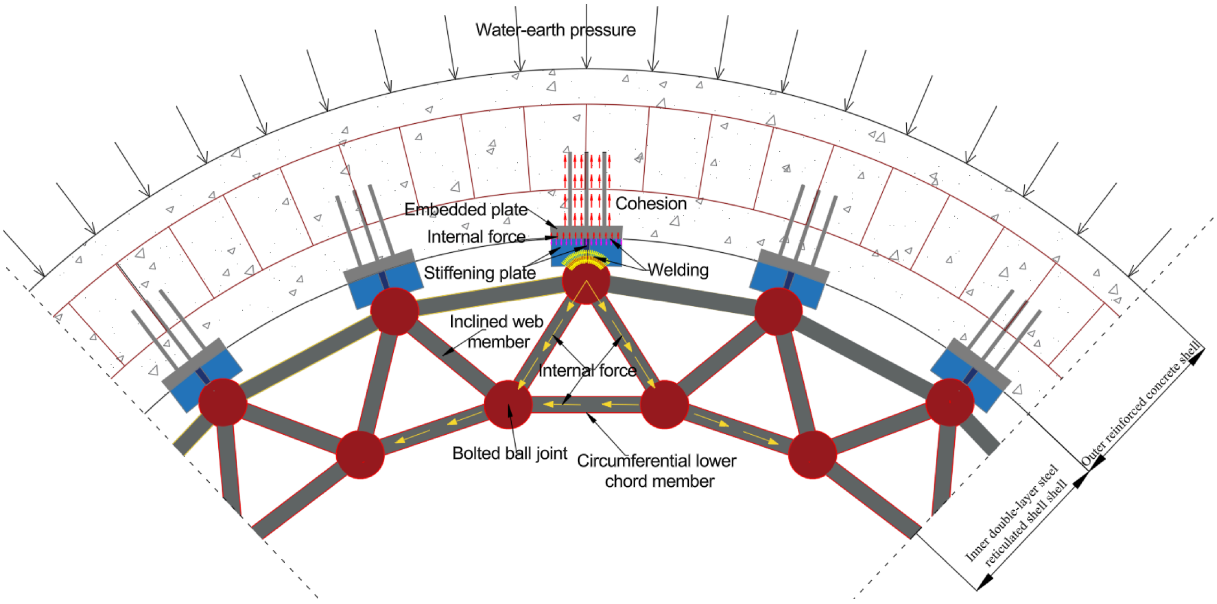


Figure 3. Load transfer path of the SCRS.

Steel–concrete synergistic mechanism: During normal service (elastic stage), strains in the outer concrete and the inner steel reticulated shell remain essentially compatible, enabling them to share external loads. The concrete primarily sustains compressive stress, while the steel shell predominantly resists tensile stresses, fully leveraging the mechanical advantages of both materials. As external loads increase to the cracking threshold, the concrete disengages from the tensile zone. The tensile stresses previously carried by the concrete are then transferred to the steel shell through interfacial shear action, allowing the steel skeleton to act as a "second line of defense" in load-bearing. This mechanism ensures that the structure retains its load capacity after concrete cracking, in contrast to the brittle, abrupt degradation typical of conventional RC segments; because no conventional RC reference ring was tested in this study, this contrast is supported by the numerical comparison reported in [25] rather than by a direct experimental comparison.

Spatial load-bearing advantages of the reticulated shell: Compared with flat steel plate strengthening or solid steel linings, the reticulated shell structure offers three key mechanical advantages: (1) Spatial load distribution: the upper chords, lower chords, and web members of the double-layer shell form a three-dimensional load-bearing system that distributes loads evenly across members and avoids local stress concentrations; (2) Lightweight efficiency: the members feature slender cross-sections and low steel consumption, reducing overall self-weight while maintaining sufficient load capacity; (3) Open configuration: the void space of the reticulated shell provides natural flow channels and mechanical interlocking interfaces for subsequent secondary concrete casting, tightly integrating the secondary lining with the original structure.

Mechanical logic of the secondary service life concept: Traditional segment strengthening requires chipping away concrete or bonding external materials, where the old–new interface relies solely on bond strength to transfer shear forces, resulting in low reliability. By pre-setting an internal steel reticulated shell, the new segment reserves "structural anchor points" for secondary strengthening. Once secondary concrete is cast, the members of the steel shell are embedded into the new matrix, creating a mechanical interlock. Meanwhile, the steel skeleton directly participates in the load-bearing of the secondary lining, establishing a three-layer composite cross-section ("original segment–steel skeleton–secondary lining"). A lower bound on the flexural stiffness of this composite cross-section is the sum of the individual layer stiffnesses computed without shear connection ($D = \sum D_i$); with

the mechanical interlock provided by the embedded steel shell and the resulting interfacial shear transfer, the actual flexural stiffness exceeds this lower bound, and this composite action makes the post-strengthening load capacity significantly higher than that of the original structure.

The foregoing analysis theoretically elucidates the synergistic action and load capacity of the new segment. Furthermore, a three-ring stagger-jointed shield tunnel model previously developed by the research group in MIDAS GTS NX demonstrates that, under identical surcharge loading, the composite segments develop markedly smaller horizontal convergence than conventional segments (38.56 mm versus more than 60 mm at the eighth load level, and 61 mm versus 100.1 mm at the twelfth load level, a reduction of about 39%) and lower bolt principal stresses (347.6 MPa versus 556.8 MPa at the eighth load level) [25]. These quantitative comparative findings provide numerical support for the mechanical analysis.

It should also be noted that the load transfer path of Figure 3 is a two-dimensional idealization of the three-dimensional structure: the ring action of the cross-section (hoop compression and flexure) is retained, whereas the three-dimensional effects of the prototype—the staggered assembly of the segmental rings, the ring-to-ring interaction through the longitudinal joints, and the longitudinal distribution of the bolted connections—are not represented. This idealization affects the characteristic values rather than the pattern of the internal forces: the alternating positive and negative bending moments along the circumference and the resulting ovalization mode (Section 4.3) are governed by the cross-sectional ring action and are therefore reproduced, whereas the absolute stiffness and capacity of the jointed prototype ring are overestimated (Sections 3.1 and 4.6). The three-dimensional evidence for the jointed configuration is provided by the three-ring stagger-jointed finite-element model of the composite segments [25].

3. Experimental Program

3.1. Specimen Design

This experiment used a shield tunnel lining from the Hangzhou Metro as the engineering prototype, featuring an outer diameter of 6700 mm, an inner diameter of 5500 mm, a width of 1200 mm, and a total thickness of 600 mm. The prototype ring comprises one key segment (20°), two adjacent segments (68.75° each), and three standard segments (67.5° each), assembled with staggered joints and M30 bolts. Constrained by the spatial dimensions and capacity of the laboratory facility, the specimens were scaled down using a geometric ratio of 1:8.6, yielding an outer diameter of 775 mm, an inner diameter of 625 mm, a width of 140 mm, and a wall thickness of 75 mm (the as-built value implied by the recorded outer and inner diameters; the strictly scaled value is 600/8.6 ≈ 70 mm). Because fabricating individual blocks with scaled bolt connections was impractical at this size, the specimen was cast as a continuous full-ring structure. This design eliminates joint effects to focus exclusively on the core load-bearing behavior of the segment body. The as-built wall thickness slightly exceeds the strictly scaled value, mirroring the as-built reinforcement, which also exceeded the strictly scaled values; both deviations bias the absolute stiffness and capacity upward, whereas the strengthening increment between the two stages of the same specimen is not confounded. The model preserves the two-layer configuration of the prototype, i.e., an outer RC layer and an inner reticulated shell within the wall.

The specimen consists of an outer reinforced concrete (RC) layer and an inner double-layer steel reticulated shell within a wall thickness of 75 mm; following the prototype proportions (a 300 mm outer RC layer and a 300 mm reticulated shell within a 600 mm wall), the design intent was an approximately equal thickness of the two layers (about 35 mm each at the 1:8.6 scale), whereas the as-built thicknesses of the individual layers were

not measured separately. For clarity, the four related quantities are distinguished as follows: the RC-layer thickness and the reticulated-shell depth denote the two constituent layers of the wall; their sum is the structural radial thickness, i.e., the wall thickness of 75 mm, which coincides with the total composite-section depth, the secondary lining being cast within the shell voids without increasing it. The steel shell is a spatial framework of inner and outer chords connected by web members, fabricated from commercially processed steel members rather than certified Q345B pipes; the measured properties of the as-built steel (an ultimate tensile strength of about 240–400 MPa across two test batches) are reported below together with those of the concrete. Due to extreme scaling limits, reproducing prototype bolted spherical joints was impractical; consequently, all members of the double-layer shell were joined by direct welding. The upper chords of the steel shell are welded to the longitudinal rebars and stirrups of the outer RC layer, ensuring that both components work cooperatively as an integral unit. Figure 4 illustrates the structural configuration (a), the fabricated steel skeleton (b), and the overall setup installed in the loading rig (c).

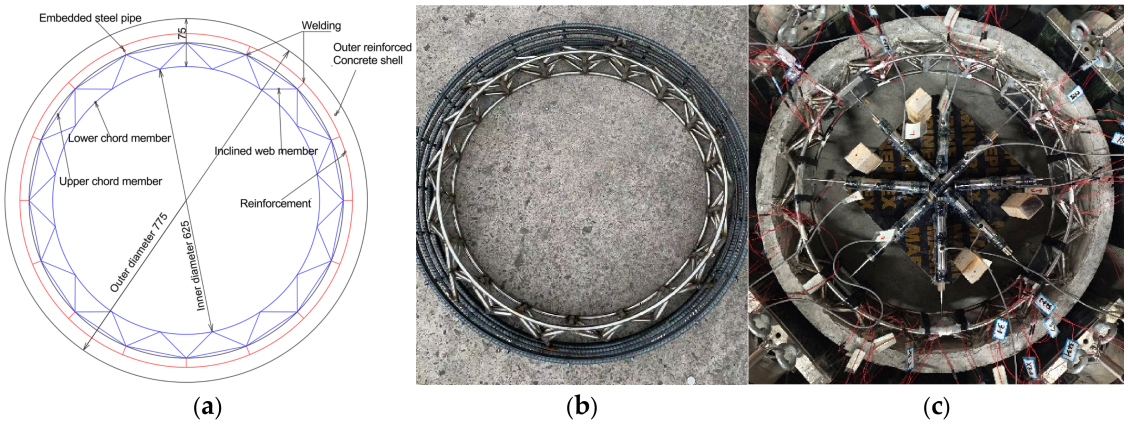


Figure 4. Photos of the specimen configuration. (**a**) Schematic diagram of the specimen configuration; (**b**) photo of the fabricated steel skeleton before loading; (**c**) overall photo of the specimen installed in the loading rig.

The initial unstrengthened specimen is designated as S-CN. Following the surcharge test and ensuing plastic deformation, a secondary lining of C40 fine-aggregate concrete was cast inside the steel shell of the damaged specimen. The reticulated framework served as a skeleton for fresh concrete, filling the internal voids without increasing overall segment thickness to form the strengthened specimen, S-CR. This directly implements the secondary service life concept. Because the segment had sustained unrecoverable plastic deformation prior to casting, it could not be restored to a true circle, leaving the geometry of S-CR slightly deviating from an ideal ring. The primary design parameters of both specimens are summarized in Table 1. A companion specimen was fabricated at the same 1:8.6 geometric scale, with a 2 mm wire mesh scaled to the same ratio replacing the outer reinforcement, and tested under the same eight-head surcharge configuration; it reproduced the same ovalization mode (vertical flattening and horizontal expansion), the same crack initiation and propagation sequence, and the same chord force distribution (lower chords in tension at the crown and invert and in compression at the springings), and it was loaded to its ultimate load, confirming that the baseline behavior reported for S-CN is reproducible rather than specimen-specific and providing failure-stage evidence beyond the terminal load of S-CN. The companion specimen is introduced here only as supporting qualitative evidence of the reproducibility of the baseline behavior; its individual test results are not reported in this paper.

Table 1. Design parameters of the specimens.

Parameter	S-CN (Unstrengthened)	S-CR (Strengthened)
Outer diameter (mm)	775	775
Inner diameter (mm)	625	625
Width (mm)	140	140
Wall thickness (mm)	75	75
Design thickness of each layer (mm)	≈35 (1:8.6 of the 300 mm prototype layer; as-built split not measured)	≈35 (1:8.6 of the 300 mm prototype layer; as-built split not measured)
Secondary lining	— —	Concrete filled within the voids of the steel reticulated shell
Steel grade (design)	Q345B/HPB300 (measured properties of the as-built materials are given in Table 2)	Q345B/HPB300 (measured properties of the as-built materials are given in Table 2)
Specimen source	Fabricated based on scale ratio	Cast with secondary concrete after the loading deformation of S-CN
Geometric shape	Standard circular	Non-standard circular (cast after loading deformation)

Table 2. Prototype design grades and measured properties of the as-built test specimens.

Material	Prototype Design Grade	As-Built Specimen (Measured)	Test Standard
Concrete (outer RC layer and secondary lining)	C40	27 MPa cubic compressive strength (nine 100 mm cubes; group means 27.6, 27.7 and 30.0 MPa)	GB/T 50081
Steel reticulated shell	Q345B	Ultimate tensile strength 402.1 MPa (first test batch, mean of four Ø10 coupons, COV 6.9%); second batch mean 237.0 MPa (COV 29.2%) with one coupon failing early; nominal grade Q345B (yield strength 345 MPa). Only the ultimate tensile strength was measured directly; the yield strength (345 MPa) and elastic modulus (206 GPa) cited for the Q345B grade are nominal design values, not measured for the as-built steel, and any comparison of the measured steel strains with this nominal yield strain is therefore approximate. Tested per GB/T 228.1.	GB/T 228.1
Reinforcement mesh	HPB300	Not separately characterized	—

Material properties are specified as follows. The concrete was hand-mixed in small batches (cement:sand:stone:water = 1:1.63:2.9:0.5 by mass) and placed through the voids of the dense steel shell, where compaction was restricted; its design strength grade is C40, while the measured 28-day cubic compressive strength of the as-cast concrete is 27 MPa on the 100 mm cube basis (nine 100 mm cubes tested in three groups, with group means of 27.6, 27.7 and 30.0 MPa, a spread of 2.4 MPa; the reported value is a conservative figure close to the two lower group means). To refer to the standard 150 mm cube strength, the 100 mm cube results are converted using a factor of 0.95 (i.e., $f_{cu,150} \approx 0.95\, f_{cu,100}$), giving an equivalent 150 mm cube strength of about 25.6 MPa. The steel reticulated shell was fabricated from commercially processed steel members rather than certified Q345B

products; its measured ultimate tensile strength is reported in Table 2. The tensile coupons were taken from the same commercially processed steel stock used to fabricate the shell members, so the measured strength characterizes the actual material of the tested ring. Eight coupons were tested in two batches of four in accordance with GB/T 228.1 [26]; the reported value is the mean of the first batch (402.1 MPa, coefficient of variation 6.9%), whereas the second batch showed pronounced scatter (mean 237.0 MPa, COV 29.2%) owing to an early coupon failure, and the first-batch mean is therefore taken as the representative tensile strength. The reinforcement mesh within the outer concrete layer employs HPB300 rebars. The design grades (C40 for the concrete and Q345B for the steel) refer to the prototype, whereas the measured values above characterize the as-built test specimens and are used throughout the analysis, consistent with the incomplete-similarity approach of Section 3.3. The ring was tested after 28 days of curing. All material tests were conducted in accordance with Metallic materials–Tensile testing (GB/T 228.1) and Standard test method for physical and mechanical properties of concrete (GB/T 50081 [27]).

Three simplifications of the scaled test warrant explicit comment, and their effects on the outputs are discussed in detail in Section 4.6. First, the geometric ratio of 1:8.6 was adopted under the capacity constraints of the laboratory facility, and the as-built wall thickness and reinforcement exceeded the strictly scaled values; the absolute stiffness and capacity reported for the tested specimen are therefore upper bounds relative to a strictly scaled model, whereas the relative strengthening increment between the two stages of the same specimen is unaffected. Second, the bolted spherical connections of the prototype were replaced by direct welding, and the segmental ring was cast as a continuous full ring, because scaled bolted joints could not be reliably fabricated; this preserves the load-transfer path of the prototype (Section 2.3, Figure 3), and because flexible joints are weak links whose opening under negative bending reduces the effective stiffness and moment capacity, the joint-free model likewise provides an upper bound on the absolute stiffness and capacity of the prototype ring. The present study should therefore be read as a proof-of-concept study of the segment body: the geometry and joint simplifications cancel in the difference between the two stages, so the strengthening increment is not confounded, while the absolute values are upper bounds for the prototype segmental ring.

3.2. Test Setup and Instrumentation

The test was conducted using a microcomputer-controlled electro-hydraulic servo full-ring segment loading system (Yantai Xintiandi Test Technology Co. Ltd., Yantai, China) at the Geotechnical Engineering Laboratory of Hangzhou City University. This facility can apply multi-directional loads under both load- and displacement-control modes. The test setup comprises a circular reaction frame, eight hydraulic actuators, a hydraulic pump unit, and a data acquisition system (Figure 5), with the overall layout illustrated in Figure 6.

Displacement measurement: Eight linear variable differential transformers (LVDTs, with a range of ±50 mm and a precision of 0.01 mm, Yantai Xintiandi Test Technology Co. Ltd., Yantai, China) were placed along the inner ring of the specimen at the actuator loading points to monitor segmental deformation.

Strain measurement: The specimen was divided into eight equal sections. Three longitudinal strain gauges (gauge length: 80 mm, Zhejiang Huangyan Testing Apparatus Factory, Taizhou, China) were mounted at the outer, middle, and inner surfaces of each section to record cross-sectional strain distributions. Additionally, two strain gauges were attached to every lower chord and diagonal web member of the steel framework to track yielding and strain evolution throughout loading. The strain acquisition system (DH3816N, Donghua Testing Technology Co., Ltd., Jingjiang, China) was used for strain data collection. Figure 7 details the instrumentation layout.

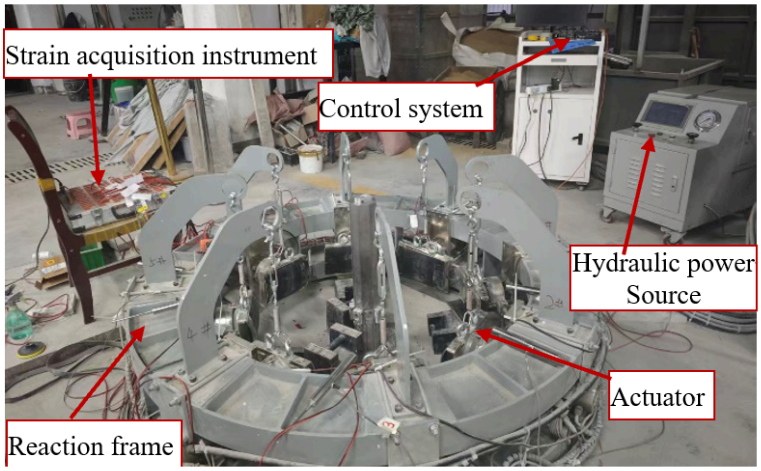


Figure 5. Photos of the test equipment.

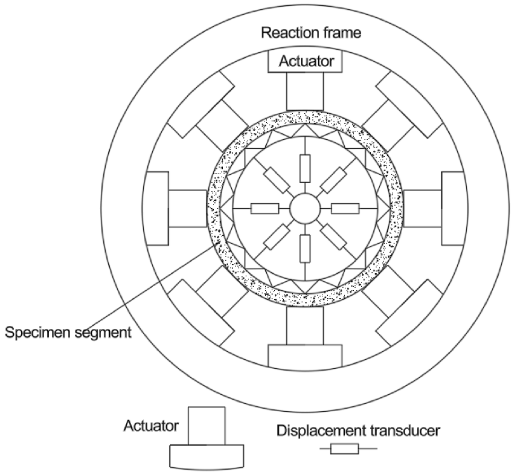


Figure 6. Schematic diagram of the experimental setup.

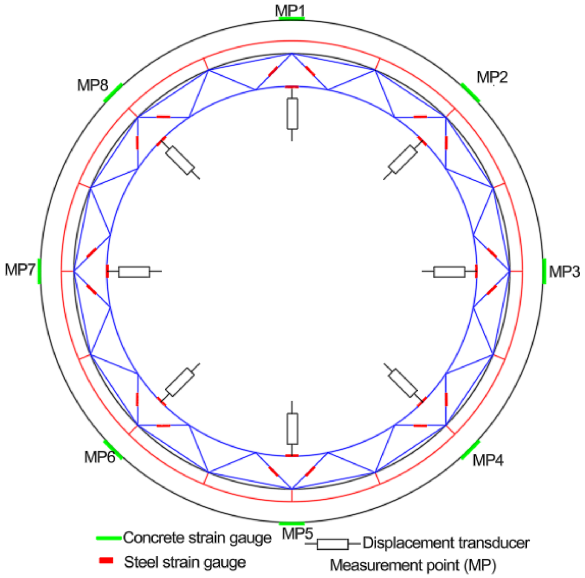


Figure 7. Schematic diagram of instrumentation layout.

All sensor data were acquired in real time at a sampling frequency of 1 Hz using an IMC-DS-2408 dynamic data acquisition system. Simultaneously, crack locations and propagation paths were manually observed and marked during loading.

3.3. Loading Protocol

Because the specimen was designed using a geometric ratio of 1:8.6, the member dimensions of the steel reticulated shell were scaled down proportionally, while the as-built reinforcement of the outer RC layer exceeded the strictly scaled value. The absolute stiffness and capacity reported for the tested specimen should therefore be regarded as upper bounds relative to a strictly scaled model, whereas the relative strengthening increment between the two stages of the same specimen is unaffected by this deviation. The as-built materials—commercially processed steel members and hand-mixed concrete—were characterized by their measured properties rather than by the prototype design grades, as reported in Section 3.1. Due to significant size effects in concrete, compressive strength varies nonlinearly with specimen dimensions, and rebar–concrete bond-slip behavior cannot be scaled through simple similarity laws. Consequently, the test could not strictly satisfy complete similarity during the elastoplastic stage. An incomplete similarity design scheme [28]—dominated by geometric similarity and based on measured material properties—was therefore adopted. The model load magnitude was determined solely by using the linear elastic similarity relationship ($S_P = L_2^S$, where S_P is the load similarity ratio and S_L represents the geometric similarity ratio) to define the reference interval for multi-stage loading, while ultimate capacity was not inversely deduced from similarity ratios. Instead, the test-derived load–displacement curves and failure modes directly reveal the mechanical behavior of the composite reticulated shell segments and serve as a benchmark for subsequent finite element validation. For reference, the model loads correspond to the following prototype equivalents. Because the load similarity ratio equals the square of the geometric similarity ratio, i.e., $(1/8.6)^2 = 1{:}74$, the model loads of 11 kN, 18.43 kN and 141.95 kN (total over the eight loading points) correspond to prototype total loads of approximately 0.81 MN, 1.36 MN and 10.5 MN, respectively. Distributed over the outer surface of the prototype ring (mid-diameter circumference $\pi \times 6.1$ m × ring width 1.2 m ≈ 23.0 m^2), these equate to equivalent uniform pressures of approximately 35 kPa, 59 kPa and 457 kPa. The elastic loading range of the model (up to the cracking load of 11 kN, i.e., about 35 kPa in prototype terms) lies well below the overburden pressures typically encountered at metro tunnel depths (of the order of 10^2 kPa), indicating that the measured elastic response is relevant to service conditions, whereas the terminal load corresponds to a condition far beyond service. Building on these principles, the multi-stage loading protocol was formulated as follows.

A two-stage loading protocol combining load and displacement control was adopted. In the elastic stage, loading was applied under load control at an increment of 0.33 kN per stage, with each load-step held for 3 min to mitigate concrete creep effects. Once the load–displacement curve exhibited distinct stiffness degradation, the system switched to displacement-control loading at a rate of 0.5 mm/min and continued until structural failure. Monotonic loading was applied to all specimens.

Test termination criteria were defined by any of the following conditions: (1) the applied load dropped below 85% of the peak load; (2) the concrete crushed and spalled; or (3) the steel members of the reticulated shell experienced local buckling or fracture.

Following the installation of specimen S-CN, each loading point achieved full contact with the segment surface, allowing loading to commence immediately. In contrast, because specimen S-CR was formed by casting secondary concrete within the deformed S-CN, its geometry deviated from a true circular ring. Consequently, uneven gaps existed between the eight radial loading points and the segment surface prior to testing. To ensure full

contact and synchronous load transfer during formal loading, a pre-tightening force was applied at each loading point. When the total pre-tightening force across all eight actuators reached 186.83 kN, the loading heads made firm contact with the segment, and the load cell readings stabilized. This pre-tightened state served as the baseline zero point for formal loading, with displacement sensors subsequently reset. All subsequent load increments and corresponding deformations were recorded relative to this initial baseline. The eight actuators were loaded synchronously under a single load regime, so only their summed force is reported and no per-actuator load table is provided. The individual force of each actuator was not recorded separately during the test, so only the summed force is known.

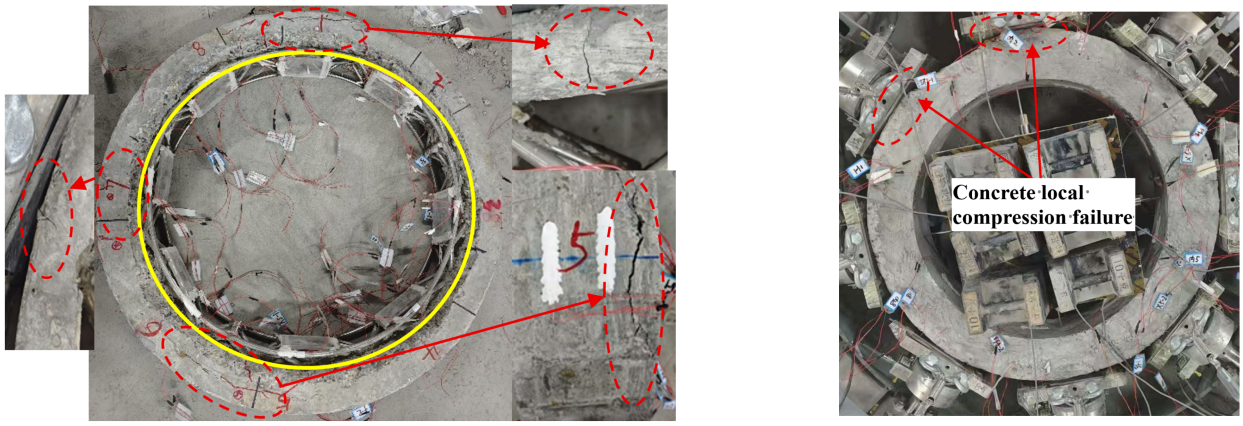
Throughout the loading process, load–displacement curves and strain data were continuously logged. Concurrently, crack initiation and propagation paths were manually tracked and marked stage by stage on the specimen surface, supplemented by photographic records.

4. Results and Analysis

4.1. Failure Modes and Crack Evolution

The loading processes of specimens S-CN and S-CR exhibited distinct differences. For the unstrengthened reference specimen S-CN, the crack development followed a sequential pattern: during the initial loading stage (0–11 kN), no visible cracks appeared on the surface, and the structure remained in an elastic state. As the load approached approximately 18 kN, transverse cracks initiated on the inner surface of the crown and propagated outward, followed by outer-surface cracks at the left and right springing's propagating inward. This distribution pattern corresponds directly to the bending moment distribution, where the crown and invert sustained positive bending moments, while the springing's experienced negative bending moments. With further load increments, the cracks multiplied and widened. At ultimate failure, the segment underwent pronounced ovalization, and the lower chord members near the mid-span of the steel framework exhibited slight local buckling.

Upon reloading following the placement of the secondary concrete lining, the strengthened specimen S-CR exhibited distinct behavior. Pre-existing cracks formed during the initial loading phase of S-CN remained tightly closed during the early stages of reloading. As the load increased, new cracks initiated along the interface between the secondary lining and the original substrate, indicating that the old–new concrete interface served as a structural weak link. Ultimate failure was characterized by local crushing of the outer concrete layer at the loading points, whereas the original steel framework remained largely intact, with no observable lower chord buckling. Figure 8 illustrates the typical failure modes of both specimens.

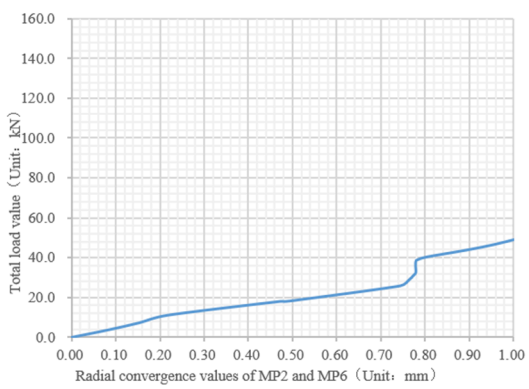


(**a**) Failure mode of specimen S-CN (**b**) Failure mode of specimen S-CR

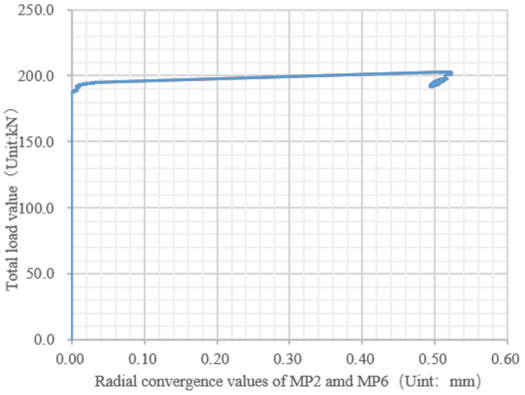
Figure 8. Failure modes of the specimens.

4.2. Load–Displacement Response

Figure 9 presents the complete load–displacement curves for specimens S-CN and S-CR. For specimen S-CN, the baseline originated at zero load, with the ordinate representing the total load across all eight loading points. For specimen S-CR, the baseline corresponded to the pre-tightened state (186.83 kN), and the ordinate reflects the net load increment (exclusive of the initial pre-tightening force) to clearly demonstrate the structural response trend during reloading. A substantial part of the pre-tightening force was likely associated with closing the initial contact gaps and contact adjustment, while some local structural deformation may also have occurred; the force acted locally at the contact interfaces and did not engage the global flexural action of the ring, as evidenced by the negligible structural displacement at seating, and the displacement baseline was reset to zero once full contact was established. The total load sustained by S-CR is thus the sum of the pre-tightening force and the net load increment (203.14 kN = 186.83 kN + 16.31 kN).



(**a**) Load–displacement curve of specimen S-CN



(**b**) Load–displacement curve of specimen S-CR

Figure 9. Load–displacement curves of the specimens: (**a**) S-CN (total load over the eight loading points, from the initial zero); (**b**) S-CR (net load after the 186.83 kN pre-tightening force, from the reset zero).

The load–displacement curve of the unstrengthened specimen S-CN (Figure 9a) exhibits distinct three-stage characteristics:

Elastic stage (0–11 kN): Load and displacement exhibit an approximately linear relationship, with displacement increasing from 0 to 1.14 mm. The segment remains in a fully elastic working state, during which the steel framework and outer concrete act synergistically.

Yield plateau stage (11–18 kN): The load increases from 11.15 kN to 18.43 kN, while displacement expands from 1.14 mm to 1.84 mm, displaying a clear yield plateau. This phase corresponds to the yielding of reinforcement within the outer RC shell and selecting members of the steel framework. This behavior aligns with strain measurements, which indicate that the lower chord reached 2388 με at 16.98 kN, exceeding the yield strain of the nominal design grade (≈1675 με for Q345B at E = 206 GPa), providing sufficient pre-failure deformation warning. Post-yield stage (18–141.95 kN): Following the yield plateau, the curve enters an ascending branch whose tangent stiffness grows with deformation.

The load increases continuously from 18.43 kN to 141.95 kN as displacement develops to 5.85 mm. The post-yield tangent stiffness increases from approximately 10 kN/mm in the elastic stage to approximately 50 kN/mm in the final stage, a magnitude that cannot be attributed to the strain hardening of the steel alone. Two structural mechanisms are considered responsible: (i) as the ring ovalized, the horizontal loading heads were progressively engaged and the contact conditions between the loading heads and the specimen evolved, modifying the effective load path; and (ii) the ring response shifted from a

bending-dominated state toward a hoop-compression-dominated state, consistent with the lower chords being predominantly in compression in the later loading stages. The test was terminated at 141.95 kN, at which point the curve maintained an upward trend without a distinct peak, indicating that the ultimate capacity of S-CN exceeds 141.95 kN.

The S-CN test was terminated at 141.95 kN before any of the termination criteria defined in Section 3.3 was met: the specimen had not failed and the load was still rising at cessation. Because the specimen was robust, the destructive program was executed in successive loading rounds with different loading-head configurations; the reported curve corresponds to the principal round, and the ultimate capacity of S-CN therefore exceeds 141.95 kN. Prior to casting the secondary concrete, the S-CN ring had already been loaded to a plastically deformed state in the initial test; the S-CR specimen therefore began its reloading from this deformed baseline, and the successive loading rounds employed different loading-head configurations, of which the reported S-CN curve is the principal round. Failure-stage evidence is provided by the companion specimen (Section 3.1), which was loaded to its ultimate load under the same eight-head surcharge configuration and exhibited the same ovalization mode and crack pattern.

Figure 9b displays the net load–displacement curve for the strengthened specimen S-CR. Because S-CR was cast within the deformed S-CN substrate, its geometry deviated from a standard circular ring, creating initial contact gaps between the radial loading heads and the segment surface. A pre-tightening force totaling 186.83 kN was applied to ensure uniform contact and synchronous load transfer. The displacement at seating is attributed jointly to the closure of the initial contact gaps and to possible equipment/operation instability—both may have contributed and cannot be distinguished from the available records—and it produced negligible structural displacement, serving as the initial baseline with displacement reset to zero. It should be noted that the displacements during the pre-tightening stage were not recorded: the total pre-tightening force of 186.83 kN (the sum over the eight actuators, at which the load-cell readings stabilized) is documented, but the corresponding displacements are not available, and the individual actuator loads at seating were not separately recorded. The resulting net load–displacement curve exhibits distinct brittle characteristics, bypassing a stable post-yield stage:

Local failure threshold (203.14 kN total load/16.31 kN net load): The specimen achieved a local failure threshold of 203.14 kN (comprising a 186.83 kN pre-tightening force and a 16.31 kN net applied load), marking the abrupt termination of its elastic-working stage. Unlike specimen S-CN, which exhibited true structural ductility, S-CR lost its load-carrying capacity suddenly at this threshold. Therefore, 203.14 kN represents a local failure threshold rather than a classic structural peak load.

Sudden load-drop stage: Upon reaching the net load of 16.31 kN (203.14 kN total load), the load dropped rapidly while displacement surged from the reset baseline to 0.51 mm. This corresponds to localized crushing of the outer RC shell beneath the eight concentrated loading points. Because the loading head area was limited, local compressive stress exceeded the local bearing strength of the concrete, triggering premature crushing and terminating the effective elastic stage. This behavior highlights the distinct brittle failure mode of S-CR compared to the stable post-yield response of S-CN. Softening stage (post-peak): The net load subsequently decreased to approximately 5 kN, while displacement stabilized around 0.50 mm. This stage reflects further compaction and stress redistribution within the crushed concrete zones at the loading points.

4.3. Theoretical Analysis of Ring Mechanics

To further reveal the mechanical essence behind the experimental phenomena, the segment was modeled as an elastic circular ring subjected to eight radial concentrated loads, as

illustrated in Figure 10a. The force method of structural mechanics was employed to derive its bending moment distribution [29]. In this theoretical analysis, the average measured load across the eight loading points served as the representative radial force. It should be noted that the theoretical model assumes a homogeneous elastic ring, which differs from the actual steel–concrete composite segment in terms of material non-uniformity, stiffness degradation post-cracking, geometric imperfections, and joint effects. Consequently, this analysis is intended not to predict exact experimental load values, but rather to reveal fundamental bending moment distribution patterns under eight-point radial loading, providing a theoretical foundation for interpreting the test phenomena. Owing to structural symmetry, a 1/8 sector model was analyzed (Figure 10b), with eight concentrated forces uniformly distributed at 45° intervals along the circumference. Under the idealized equal-load assumption the ring is periodic with a 45° repeating unit, so the 1/8 sector is the exact repeating unit and enlarging the model to a 1/4 or 1/2 sector would yield identical results; the dispersed measured loads break this symmetry, in which case a full-ring model would be required, but the sign pattern of the bending moments—the qualitative basis of the present analysis—is insensitive to this refinement. At the planes of symmetry, the rotation angle and shear force vanish. Selecting the bending moment at the symmetry plane as the redundant unknown force X_1, the canonical equation of the force method is expressed as:

$$\delta_{11}X_1 + \Delta_{1P} = 0 \tag{1}$$

where δ_{11} is the displacement along the direction of the redundant force caused by a unit redundant bending moment, and Δ_{1P} is the displacement along the direction of the redundant force caused by external loads on the primary system. Considering only the contribution of the bending moment to deformation, the integration is performed along the 1/8 circular arc:

$$\delta_{11} = \int \frac{1_2^{\overline{M}}}{EI} ds \tag{2}$$

$$\Delta_{1P} = \int \frac{\overline{M}_1 M_P}{EI} ds \tag{3}$$

where $\overline{M}_1$ is the bending moment at any cross-section of the primary structure under a unit redundant load, M_P is the bending moment caused by external loads on the primary system, E is the elastic modulus of the material, and I is the cross-sectional moment of inertia. After solving the force method equation for X_1, the final bending moment M at any cross-section is obtained.

$$M = X_1 \cdot \overline{M}_1 + M_P \tag{4}$$

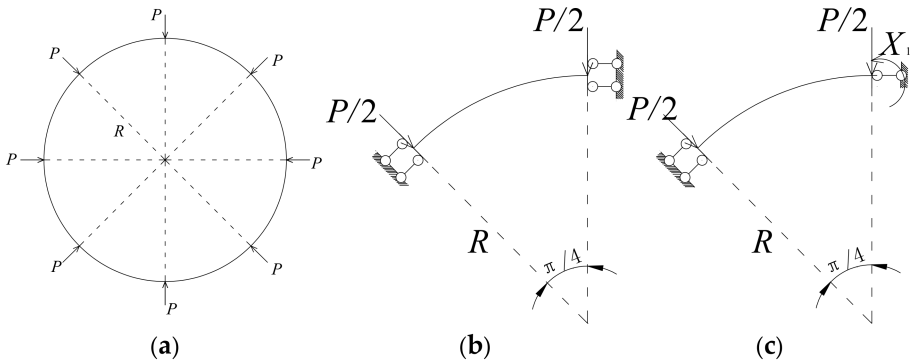


Figure 10. Force method analysis model. (**a**) The whole model of ring under eight-point radial loading; (**b**) Symmetrical 1/8 ring; (**c**) Primary system of the force method.

Force method calculations indicate that under eight-point radial loading, the bending moment of the segmental ring exhibits an alternating positive and negative distribution

along the circumference (Figure 11). Cross-sections at the loading points experience positive bending moments (inner tension), whereas intermediate sections between adjacent loading points undergo negative bending moments (outer tension), with inflection points (zero bending moment) located between them. This alternating moment pattern dictates the overall deformation behavior: sections subjected to positive bending concave inward, while those under negative bending bulge outward, collectively resulting in structural ovalization.

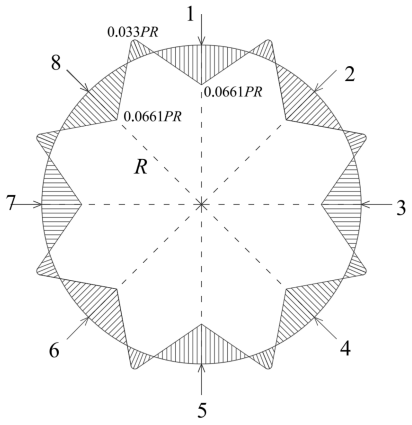


Figure 11. Bending moment diagram of the segment.

Experimental observations show good qualitative agreement with this theoretical prediction. During loading, the segment exhibited an ovalization deformation mode characterized by "vertical flattening and horizontal expansion," as illustrated in Figure 12. Inward radial displacements are defined as positive (+), and outward radial displacements as negative (−). Accordingly, displacements at the vertical loading points (measuring points 1 and 5) developed inward (+), whereas those at the horizontal measuring points (points 3 and 7) developed outward (−). The measuring-point displacements grew with the load level; the point-by-point records are presented in Figure 12, and the loading-point displacement history is given in Figure 9a. The inward displacements at the vertical measuring points reduced the vertical height of the segment, while the outward displacements at the horizontal measuring points increased its horizontal width.

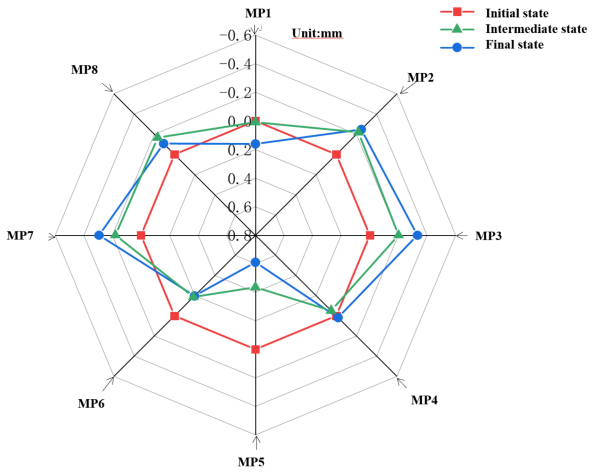


Figure 12. Deformation diagram of the specimen S-CN. (Note: In Figure 12: Positive and negative values represent inward and outward radial displacements, respectively.).

Although some dispersion exists in the measured loads among the eight points, all loads are directed radially inward. Treating their average value as an equivalent radial

load does not fundamentally alter the general pattern of the bending moment distribution, affecting only the specific characteristic values. Furthermore, measuring points 3 and 7 are located at horizontal loading points. While the bending moment diagram indicates positive bending moments (a local tendency to concave inward) at these positions, the experimentally measured displacements were outward. This phenomenon is governed by the overall deformation mode: vertical loads induce horizontal thrust via the arch effect, causing the segment to expand globally in the horizontal direction. This global expansion displacement significantly exceeds the local inward concaving displacement induced by bending. Consequently, the final outward bulge represents a superposition where global ovalization dominates over the local bending component. It should be emphasized that the equal-load assumption is an idealization: the loads measured at the eight actuators were dispersed, and the observed two-fold ovalization indicates that the vertical loading heads carried a larger share of the total load than the horizontal ones—precisely the condition under which the arch effect invoked above can operate. The agreement between the force-method analysis and the test is therefore qualitative, concerning the deformation mode and the sign pattern of the bending moments, rather than a point-by-point match of characteristic values.

The theoretical bending moment characteristics also explain the locations and propagation sequence of strains within the lower chord members of the inner steel framework. The theoretical maximum positive bending moment sections coincide with the loading points, corresponding precisely to the high tensile stresses observed at measuring points 1 and 5 during the test (Figure 13).

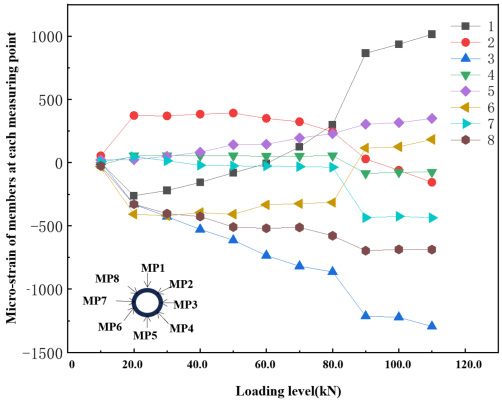


Figure 13. Strains of the lower chord members of the reticulated shell of specimen S-CN at the eight instrumented measuring points during the early loading stages (horizontal axis: loading level in kN, as recorded during the test; the plotted strains range from about −1500 με to about 1000 με, with the maximum plotted value remaining below the nominal yield strain of the Q345B grade, ≈1675 με at E = 206 GPa).

4.4. Strain Evolution Characteristics

Strain data from specimen S-CN validate the failure mechanisms deduced from the load–displacement curves. Reliable strain readings for both the concrete and the lower chord members of the steel framework were successfully acquired for specimen S-CN. (Note: Strain gauges on specimen S-CR were damaged during the secondary concrete placement, yielding no valid data.).

For specimen S-CN, the endpoint of the elastic stage (11 kN) corresponds to a concrete surface strain of 88 με which approaches the ultimate tensile strain of C40 concrete, indicating that concrete cracking triggers the conclusion of the elastic stage. Within the yield plateau stage (11–18 kN), strain in the lower chord members continued to increase, reaching 2388 με at a load of 16.98 kN. This exceeds the yield strain of the steel under the nominal

design grade (≈1675 με for Q345B at E = 206 GPa), confirming that the physical essence of the yield plateau is the plastic yielding of the steel framework. These strain measurements confirm microscopically that the failure of S-CN was governed by steel yielding, exhibiting a characteristic ductile failure mode.

4.5. Experimental Verification of Steel–Concrete Synergistic Working Mechanism

Based on the strain data of specimen S-CN presented in Section 4.4, the effectiveness of the steel–concrete synergistic working mechanism (detailed in Section 2.3) is experimentally validated. In the elastic stage (0–11 kN), the strain discrepancy between the outer concrete and the inner steel framework remained under 10% at the instrumented locations, confirming that loads were efficiently transferred from the outer RC shell to the inner steel framework through the welded connections between the upper chords and the shell reinforcement (Section 3.1). The load transfer pathway remained unobstructed, enabling cooperative deformation of both components. The concrete strain at the conclusion of the elastic stage (11 kN) reached its cracking threshold (88 με). Subsequently, the strain growth rate of the concrete decelerated markedly, whereas that of the steel members accelerated, increasing progressively from below 1000 με to 2388 με at 16.98 kN. This evolutionary pattern confirms that following concrete cracking, tensile stresses redistributed to the outer reinforcement and the inner steel framework, establishing a robust dual-protection mechanism. Once the steel members attained their yield strain, the load–displacement curve transitioned from the yield plateau into the post-yield stage. Figure 13 presents the early-stage gauge records, whose maximum plotted value (about 1000 με) remains below the nominal yield strain of the Q345B grade, ≈1675 με at E = 206 GPa; the maximum recorded reading of 2388 με occurred at the yield load of 16.98 kN.

For clarity, the maximum recorded steel strain (2388 με) was observed at one of the instrumented lower-chord measuring points and was reached at the yield load of 16.98 kN; this point lies beyond the early-stage range plotted in Figure 13.

For specimen S-CR, although internal strain records were unavailable due to gauge damage, its macroscopic behavior—evidenced by enhanced elastic stiffness (a displacement increment over the net loading range that remained on the order of the LVDT precision, indicating a markedly stiff response)—is consistent with the lower-bound stiffness superposition discussed in Section 2.3. The secondary concrete placement restored cross-sectional integrity and increased structural rigidity, supporting the secondary service life concept. Because the S-CR stage was initiated from a pre-tightened state of 186.83 kN with the displacement sensors reset to zero, the small displacement increment characterizes the incremental response after re-contact rather than the absolute deformation from an unstressed state; the stiffness comparison with S-CN should therefore be read as a qualitative indicator.

4.6. Discussion

Table 3 summarizes the key characteristics of the load–displacement responses for the S-CN and S-CR specimens. Specimen S-CN exhibits a distinct three-stage behavior comprising the elastic stage, yield plateau, and post-yield stage, achieving a terminal load exceeding 141.95 kN with the curve continuing upward at test cessation, so that the ultimate capacity exceeds 141.95 kN (a lower bound). In contrast, specimen S-CR demonstrates a notable enhancement in elastic stiffness following secondary concrete infilling within the steel framework voids, reaching a maximum total load of 203.14 kN, which represents a local failure threshold governed by concrete crushing beneath the loading heads rather than a classic structural peak load.

Table 3. Comparison of load–displacement curve characteristics between specimens S-CN and S-CR.

Comparison Item	S-CN (Unstrengthened)	S-CR (Strengthened)
Initial state	0 kN	186.83 kN (seating force)
Elastic stage characteristics	0 → 11 kN, displacement 0→ 1.14 mm	0 → 16.31 kN (net increment); displacement negligible (within LVDT precision after pre-tightening)
Yielding/Instability characteristics	Yield plateau (11→ 18 kN, displacement continues to increase)	Sudden change (at 16.31 kN, displacement 0.0 → 0.51 mm)
Terminal load/Local failure threshold	>141.95 kN (test terminated, peak not reached; lower bound)	203.14 kN (total load; local failure threshold)
Peak displacement	>5.85 mm (from the initial zero)	0.51 mm (from the reset baseline after 186.83 kN pre-tightening)
Post-peak behavior	Continuous ascent	Sharp decline (local compression)
Elastic stiffness	Baseline	Significantly improved
Cause of termination	Test termination	Local compression of outer concrete (concentrated loading)

Synthesizing the failure modes, load–displacement responses, and synergistic mechanism analyses, the performance divergence between S-CN and S-CR is fundamentally governed by distinct control mechanisms. S-CN was governed by flexural tension: following outer concrete cracking, the external reinforcement and inner steel framework established a robust dual-protection mechanism. Upon attaining yield strain, the framework entered the yield plateau and subsequently sustained loads through structural action beyond yield (Section 4.2), exhibiting ductile failure. Conversely, S-CR was governed by localized compression. Following secondary concrete placement, overall structural stiffness improved markedly; however, the eight-point concentrated forces generated excessively high local compressive stresses, triggering premature crushing of the outer concrete. Because this failure mode was localized in compression, the outer reinforcement and steel framework could not mitigate it, resulting in a brittle structural manifestation.

The ductile failure of S-CN confirms the pronounced load-bearing performance of the novel steel–concrete composite reticulated shell segments under flexural tension. The sharp drop in S-CR stems strictly from localized crushing beneath the loading points rather than a global loss of structural capacity. Under true uniform loading conditions in actual engineering, such localized crushing would be absent, indicating that the practical ultimate capacity of S-CR is likely higher. This test validates the feasibility of the secondary service life concept for enhancing structural stiffness while highlighting the limitations of concentrated loading methodologies for composite structures. Future research should adopt uniform loading setups to fully evaluate the load-bearing potential of strengthened segments.

The strengthening effect is quantified by multiple independent indicators rather than by a single capacity value. First, the pre-existing cracks formed during the S-CN stage remained tightly closed during the early reloading of S-CR, directly evidencing recovered cross-sectional integrity. Second, measured from its own zero baseline, the elastic response

of S-CR (a 16.31 kN net increment, on the order of the LVDT precision) was markedly stiffer than that of S-CN (11 kN at 1.14 mm), so this contrast is best read as a qualitative indicator of recovered stiffness. Third, the failure mode shifted from ductile flexural-tension failure to local compression crushing beneath the loading heads, indicating that the flexural demand of the reloaded ring remained far below the enhanced capacity of the composite section. Fourth, the measured response is consistent with the lower-bound stiffness prediction of Section 2.3, according to which the sum of the individual layer stiffnesses computed without shear connection constitutes a lower bound on the flexural stiffness of the composite cross-section; although full composite action was not independently verified experimentally, the observed enhancement is consistent with the actual stiffness exceeding this lower bound under composite action. The concurrence of these independent observations makes the conclusion of strengthening effectiveness robust.

Two simplifications of the scaled test warrant comment. First, the bolted spherical joints of the prototype were replaced by direct welding because they could not be reliably fabricated at the 1:8.6 scale. This changes the connection type but preserves the load-transfer path of the prototype (outer RC shell → embedded connection plates → joints → inner reticulated shell; Section 2.3, Figure 3): the upper chords are welded to the longitudinal reinforcement and stirrups of the outer RC layer, so the steel–concrete composite action and the interfacial shear transfer are retained. Because bolted joints are flexible weak links whose opening under negative bending reduces the effective stiffness and moment capacity of a segmental ring, the joint-free model provides an upper bound on the absolute stiffness and capacity of the prototype ring. Moreover, since S-CN and S-CR share an identical joint-free configuration, this simplification cancels in the difference between the two stages and does not confound the strengthening increment. Joint effects on the absolute stiffness of the prototype cannot be quantified from this test alone and are recommended for future work, for example tests with scaled bolted joints or finite-element models with joint elements.

Several limitations should also be noted. First, the eight-point concentrated loading differs from the uniform earth pressure encountered in practice; the local crushing beneath the loading heads therefore limits the measured capacity of S-CR, which should be interpreted as a lower bound for the strengthened system under uniform pressure. Second, no independent undamaged control specimen with a secondary lining was tested; the strengthening effect was instead evaluated through the self-controlled (paired) design of the two stages of the same specimen, which eliminates specimen-to-specimen scatter but relies on the comparability of the two baselines. Third, the as-built reinforcement of the tested specimen exceeded the strictly scaled value, so its absolute stiffness and capacity are upper bounds relative to a strictly scaled model; the companion specimen, in which the outer reinforcement was provided by a wire mesh scaled to the same ratio, reproduced the baseline behavior but was not strengthened. Fourth, the strain gauges on S-CR were damaged during the secondary concrete placement, so the internal force redistribution within the strengthened section could not be measured directly. Finally, the as-built materials were characterized by measured properties rather than the prototype design grades; all mechanistic conclusions are tied to these measured values, and the yield interpretation remains valid under either the nominal or the measured properties (Section 4.4).

The old–new concrete interface and the long-term durability of the concept warrant explicit discussion. In the S-CR test, new cracks initiated along the interface between the secondary lining and the original substrate, indicating that this interface is a structural weak link. From a materials point of view, the secondary concrete was cast against a rigid, cracked substrate, and the restrained shrinkage of the fresh concrete is considered a likely cause of these interface cracks. The documented surface preparation was limited to removing the foam used to block the shell voids and wiping the surfaces with alcohol; no roughening or

bonding agents were reported. The secondary lining was designed as C40 fine-aggregate concrete, but its measured strength and its age at the time of the reloading test were not recorded, which limits the quantitative interpretation of the interface behavior. Looking beyond the test, the steel reticulated shell remains exposed inside the tunnel for decades before the secondary lining is cast; corrosion protection, fire protection, and provisions for inspection of this exposed skeleton are therefore essential for the practical implementation of the concept and should be addressed in future design guidelines.

5. Conclusions

To address the performance degradation of conventional tunnel linings, this study proposes novel steel–concrete composite reticulated shell segments based on the secondary service life concept. Through full-ring structural testing, the load-bearing performance and secondary strengthening mechanisms were systematically investigated. The primary conclusions are drawn as follows:

Pronounced Baseline Ductility: In the initial, unstrengthened state, the segment exhibits pronounced ductile behavior characterized by three distinct phases: the elastic stage, yield plateau, and post-yield stage. The prominent yield plateau (11–18 kN) provides a crucial deformation warning prior to structural failure. Upon test cessation at a terminal load of 141.95 kN—a lower bound on the ultimate capacity—the curve was still ascending, demonstrating continued load-bearing potential without catastrophic failure.

Progressive Load-Bearing Mechanism: The pronounced ductility of the structure is governed by a dual tension-bearing system comprising outer reinforcement and the inner steel framework. Following initial concrete cracking at 88 με, the outer rebars and inner steel framework sequentially engage to sustain tensile stresses. The structural yield plateau corresponds directly to the plastic yielding of the framework (recorded at 2388 με under 16.98 kN). This progressive activation effectively prevents brittle failure and aligns with the alternating positive and negative bending moments governing global ring ovalization.

Efficacy of the Secondary Service Life Concept: Casting secondary concrete into the voids of the steel framework enhances both structural stiffness and load-bearing capacity. The strengthened specimen (S-CR) demonstrated a very small deformation (on the order of the LVDT precision) over the 16.31 kN net load increment and reached a maximum total load of 203.14 kN. This value is a local failure threshold governed by concrete crushing beneath the concentrated loading heads rather than a structural peak load, whereas the unstrengthened segment (S-CN) attained a terminal load of 141.95 kN (a lower bound on its ultimate capacity) before test cessation. Because the two load levels arise from different failure mechanisms, the enhancement in load-carrying performance is best interpreted as a qualitative indication of the potential of the secondary concrete to improve the structural response and load-carrying performance of the ring, rather than as a direct quantitative capacity gain. This supports the viability of the secondary service life concept for in-situ structural renewal.

Testing Limitations and Future Work: The post-peak brittle failure observed in the strengthened specimen stemmed strictly from localized concrete crushing beneath the concentrated loading points rather than a global loss of structural capacity. Because such severe stress concentrations are largely absent under authentic, uniform earth-pressure conditions, the true ultimate capacity of the strengthened segment in engineering practice is likely higher. Future investigations utilizing uniform loading apparatuses (e.g., hydraulic bladders) are recommended to fully evaluate the ultimate load-bearing performance of the composite structure. In addition, the joint-free configuration of the scaled test provides an upper bound on the absolute stiffness and capacity of the prototype ring, whereas the strengthening increment itself is not confounded by this simplification because it cancels

between the two stages of the same specimen. Furthermore, the as-built specimens were fabricated from commercially processed steel and hand-mixed concrete rather than the prototype design grades (Q345B and C40); the measured properties were used throughout the analysis, and the yield interpretation of Section 4.4 holds under both the nominal and the measured material properties. The present experiment demonstrates short-term mechanical recovery under monotonic loading as a proof of concept and does not by itself validate a secondary service life, which would additionally involve fatigue and cyclic loading, long-term durability, water tightness, interface degradation and joint behavior; these aspects, together with a full-scale finite-element model of the prototype segment (extending the three-ring stagger-jointed model of [25]) and further testing under uniform earth-pressure loading, are identified as future research needs.

Author Contributions: Conceptualization, L.X. and G.W.; methodology, L.X.; validation, L.X.; formal analysis, L.X.; investigation, L.W.; resources, G.W.; data curation, L.W.; writing—original draft preparation, L.W.; writing—review and editing, L.X.; supervision, G.W.; project administration, G.W.; funding acquisition, G.W. All authors have read and agreed to the published version of the manuscript.

Funding: This research was funded by the National Natural Science Foundation of China (Grant No. 52578490) and supported by the Zhejiang Provincial Natural Science Foundation of China (Grant No. LMS26E080035).

Data Availability Statement: The raw experimental data generated in this study are not publicly available due to laboratory management restrictions, but are available from the corresponding author upon reasonable request.

Conflicts of Interest: The authors declare no conflict of interest.

References

1. China Urban Subterranean Space Development Blue Book Editorial Committee. 2025 China Urban Underground Space Development Blue Book. 2025. Available online: http://files.hy.csrme.com/ftp/data/User/csrme/home/ftp/BlueBook2025/mobile/index.html#p=46 (accessed on 15 December 2025).
2. Chen, X.; Su, D.; Wu, Z.; Han, K.; Lin, X.; Cao, X.; Chen, W. Resilience development path and strategy of underground space in megacities in China. *Bull. Chin. Acad. Sci.* **2026**, *41*, 244–259. [CrossRef]
3. Yi, R.; Zhang, L.N. Underground space economy: Industrial basis and strategic path under the background of intensive development. *Bull. Chin. Acad. Sci.* **2026**, *41*, 233–243. [CrossRef]
4. Park, J.; An, J.-B.; Ko, K.-W.; Cho, G.-C. Soil-tunnel interaction for segmental linings with non-planar longitudinal joints via centrifuge modeling. *Tunn. Undergr. Space Technol.* **2026**, *168*, 107206. [CrossRef]
5. Mu, H.; Feng, K.; Yang, S.; Li, J.; Tang, R.; Guo, W.; Zhou, Y.; He, C. Investigation on internal force transmission and failure characteristics of segmental linings for super-large cross-section shield tunnels. *Structures* **2025**, *74*, 108564. [CrossRef]
6. Zhang, T.; He, B.; Chen, Z.; Li, X.; Zheng, G. Modelling progressive failure of segmental linings in shield tunnels. *J. Civ. Eng. Manag.* **2025**, *31*, 596–607. [CrossRef]
7. Zhang, W.; Qi, J.; Zhang, G.; Niu, R.; Zhang, C.; He, L.; Lyu, J. Full-scale experimental study on failure characteristics of the key segment in shield tunnel with super-large cross-section. *Tunn. Undergr. Space Technol.* **2022**, *129*, 104671. [CrossRef]
8. Zhang, J.; Liu, X.; Sun, Z.; Li, Y.; Cao, G. Statistical analysis of deformation and disease of shield tunnel under different stratum conditions. *Chin. J. Undergr. Space Eng.* **2025**, *21*, 320–328. [CrossRef]
9. TRB Committee AFF60. *Investigation of the Tunnel Ceiling Collapse in the Central Expressway in Japan*; Transportation Research Board: Washington, DC, USA, 2012.
10. Chen, R.; Fan, M.; Cheng, H.; Wu, H.; Zhang, Y.; Gao, B.; Ruan, S. Analyzing the strengthening effect of steel-ultra high performance concrete composite on segmental linings. *J. Zhejiang Univ.-Sci. A* **2025**, *26*, 558–572. [CrossRef]
11. Yu, Y.; Sun, Y.; Wang, J. The mechanical behavior of a shield tunnel reinforced with steel plates under complex strata. *Buildings* **2025**, *15*, 2722. [CrossRef]
12. Feng, X.; Liu, D.; Guo, Y.; Zhong, F.; Zuo, J.; Liu, W. Research on mechanical performance of longitudinal joints in segmental tunnel linings strengthened by fiber-reinforced plastic grid with polymer-cement-mortar method. *Front. Struct. Civ. Eng.* **2024**, *18*, 1610–1625. [CrossRef]

13. Liu, X.; Jiang, Z.; Mang, H.A. Experimental investigation of the bearing capacity of deformed segmental tunnel linings strengthened by a special composite structure. *Struct. Infrastruct. Eng.* **2023**, *19*, 147–163. [CrossRef]
14. Zhang, J.-L.; Liu, X.; Ren, T.-Y.; Shi, Y.-M.; Yuan, Y. Numerical analysis of tunnel segments strengthened by steel–concrete composites. *Undergr. Space* **2022**, *7*, 1115–1124. [CrossRef]
15. Chen, R.-P.; Gao, B.-Y.; Ruan, S.-Q.; Wu, H.-N.; Fan, M.; Feng, D.-L. Experimental study on the mechanical behavior of segmental joints of shield tunnels strengthened by a steel plate-UHPC composite. *Tunn. Undergr. Space Technol.* **2024**, *144*, 105536. [CrossRef]
16. Sun, Y.Z.; Yu, Y.; Wang, J.C.; Ye, Y.L.; Tan, Q.Y. Mechanical properties of linings of shield tunnel strengthened by steel plates considering interface effects. *Chin. J. Geotech. Eng.* **2022**, *44*, 343–351. [CrossRef]
17. Liu, D.; Yao, X.; Dai, Q.; Tian, C.; Zheng, J. Debonding and control of shield tunnel strengthened with thin plate. *Struct. J.* **2025**, *122*, 17–28. [CrossRef]
18. Tian, C.; Huang, L.; Liang, Y.; Gao, W. Damage evolution and toughening mechanism of shield tunnel segments strengthened by epoxy-bonded thin plates considering interface effects. *Comput. Geotech.* **2025**, *184*, 107309. [CrossRef]
19. Meng, G.; Li, H.; Liu, G.; Han, Y.; Zhang, Y.; Huang, C. Steel fiber reinforced concrete segments for shield tunnels: A comprehensive review of mechanical performance, design methods and future directions. *Buildings* **2025**, *15*, 4354. [CrossRef]
20. Zhang, F.; De Corte, W.; Taerwe, L.; Cao, W.; Liu, X. A study on the bending stiffness of reinforced concrete tunnel segments with added steel fibers. *Materials* **2025**, *18*, 48. [CrossRef] [PubMed]
21. Jianhong, W.; Zhipeng, X.; Chaojun, C.; Huibin, S.; Shixing, W.; Yu, T.; Yunfa, H.; Jian, C. Experimental study on flexural performance of steel fiber reinforced concrete and application of large-diameter shield segments. *J. Basic Sci. Eng.* **2025**, *33*, 244–255. [CrossRef]
22. Hou, M.; Feng, J.; Shi, H.; Jiang, R.; Zhu, H.; Fan, H. Two-scale basalt fibers reinforced concrete shield tunneling segments for underground constructions. *Tunn. Undergr. Space Technol.* **2025**, *157*, 106383. [CrossRef]
23. Hou, M.; Zhu, H.; Fan, H. Short BFRP fibers and BFRP rebars reinforcements to tailor mechanical performances of shield tunnel segments and failure analyses. *Arch. Civ. Mech. Eng.* **2026**, *26*, 72. [CrossRef]
24. Feng, H.; Su, P.; Su, C.; Xin, X.; Chen, Y.; Bai, Y. Design approach for flexural properties of engineered geopolymer composite shield tunnel segments reinforced with GFRP bars. *Tunn. Undergr. Space Technol.* **2025**, *162*, 106639. [CrossRef]
25. Liu, X.; Liu, Y.; Jiang, Z.; Wang, J.; Mang, H.A. Numerical analysis of mechanical performance of novel steel-concrete composite shield segments. *Cryog. Archit. Technol.* **2024**, *46*, 91–96. [CrossRef]
26. *GB/T 228.1-2021*; Metallic Materials—Tensile Testing—Part 1: Method of Test at Room Temperature. Standardization Administration of the People's Republic of China (SAC): Beijing, China, 2021.
27. *GB/T 50081-2019*; Standard for Test Methods of Concrete Physical and Mechanical Properties. China Architecture & Building Press: Beijing, China, 2019.
28. Wei, G.; Feng, F.; Huang, S.; Xu, T.; Zhu, J.; Wang, X.; Zhu, C. Full-scale loading test for shield tunnel segments: Load-bearing performance and failure patterns of lining structures. *Undergr. Space* **2024**, *20*, 197–217. [CrossRef]
29. Chen, S.F.; Shen, G.H.; Chen, Y.; Wan, H.P. *Structural Mechanics I*; Higher Education Press: Beijing, China, 2025.

Disclaimer/Publisher's Note: The statements, opinions and data contained in all publications are solely those of the individual author(s) and contributor(s) and not of MDPI and/or the editor(s). MDPI and/or the editor(s) disclaim responsibility for any injury to people or property resulting from any ideas, methods, instructions or products referred to in the content.